

# Atomistic Texture of Amorphous Manganese Oxides for Electrochemical Water Splitting Revealed by Ab Initio Calculations Combined with X-ray Spectroscopy

Giuseppe Mattioli,<sup>\*,†</sup> Ivelina Zaharieva,<sup>‡</sup> Holger Dau,<sup>‡</sup> and Leonardo Guidoni<sup>¶</sup>

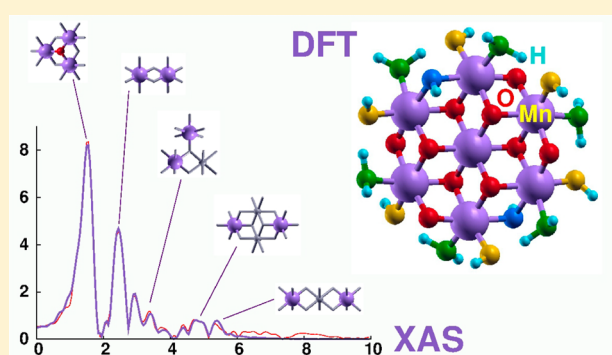
<sup>†</sup>Istituto di Struttura della Materia del CNR, v. Salaria Km 29,300 - C.P. 10 I-00015 Monterotondo Stazione, Rome, Italy

<sup>‡</sup>Fachbereich Physik, Freie Universität Berlin, Arnimallee 14, 14195 Berlin, Germany

<sup>¶</sup>Dipartimento di Scienze Fisiche e Chimiche, Università degli Studi de L'Aquila, Via Vetoio 2, Coppito, I-67100 L'Aquila, Italy

**S** Supporting Information

**ABSTRACT:** Amorphous transition-metal (hydr)oxides are considered as the most promising catalysts that promote the oxidation of water to molecular oxygen, protons, and “energized” electrons, and, in turn, as fundamental parts of “artificial leaves” that can be exploited for large scale generation of chemical fuels (e.g., hydrogen) directly from sunlight. We present here a joint theoretical–experimental investigation of electrodeposited amorphous manganese oxides with different catalytic activities toward water oxidation (MnCats). Combining the information content of X-ray absorption fine structure (XAFS) measurements with the predictive power of ab initio calculations based on density functional theory, we have been able to identify the essential structural and electronic properties of MnCats. We have elucidated (i) the localization and structural connection of Mn(II), Mn(III), and Mn(IV) ions in such amorphous oxides and (ii) the distribution of protons at the MnCat/water interface. Our calculations result in realistic 3D models of the MnCat atomistic texture, formed by the interconnection of small planar Mn-oxo sheets cross-linked through different kinds of defective Mn atoms, isolated or arranged in closed cubane-like units. Essential for the catalytic activity is the presence of undercoordinated Mn(III)O<sub>5</sub> units located at the boundary of the amorphous network, where they are ready to act as hole traps that trigger the oxidation of neighboring water molecules when the catalyst is exposed to an external positive potential. The present validation of a sound 3D model of MnCat improves the accuracy of XAFS fits and opens the way for the development of mechanistic schemes of its functioning beyond a speculative level.



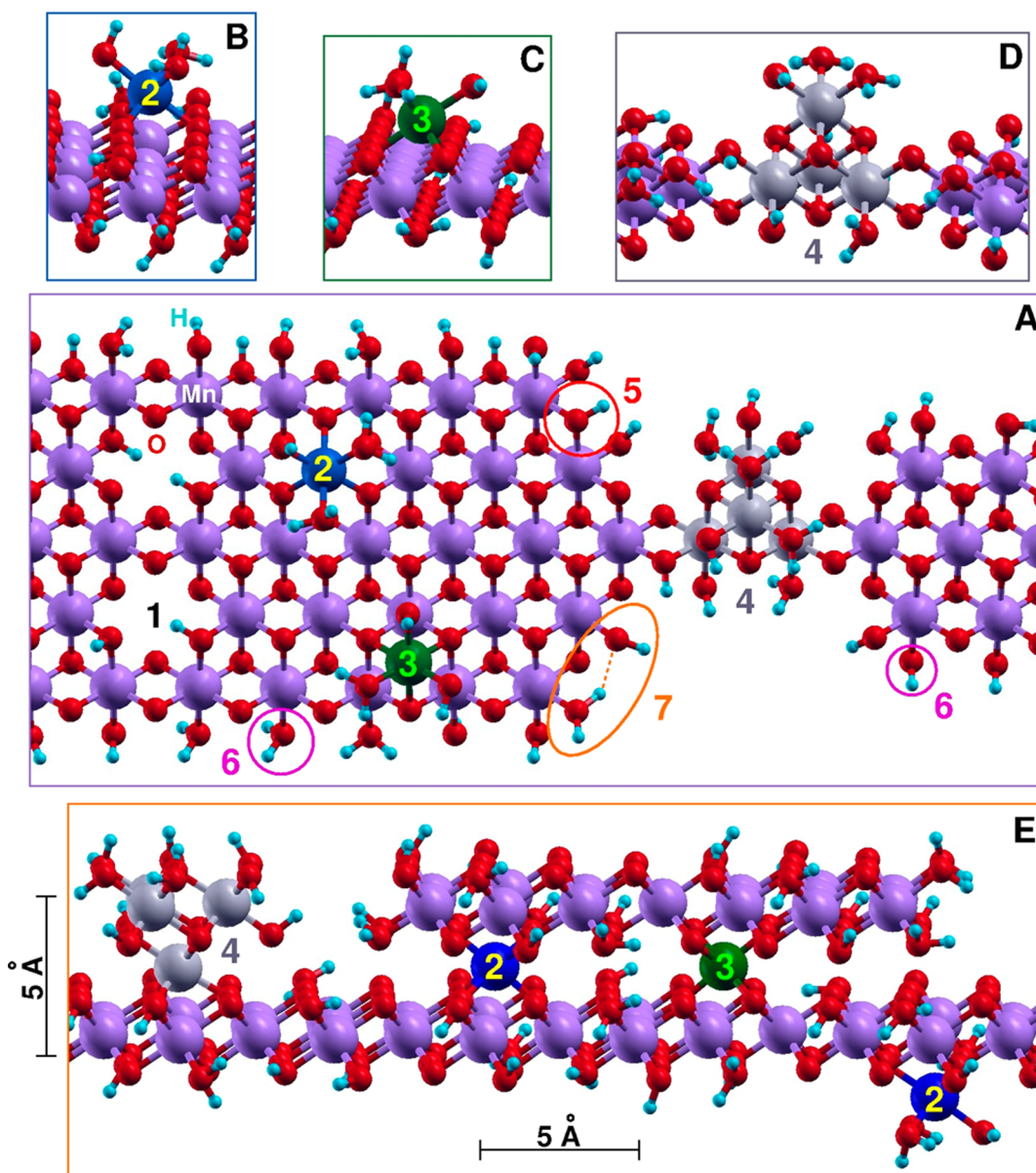
## 1. INTRODUCTION

Direct conversion of solar energy into chemical fuel represents a primary objective in the endeavor to address the globally growing energy demand in a sustainable way. This process is clean and carbon neutral, and a relevant amount of chemical energy can be stored and used when needed. Nature addresses this task everyday by oxygenic photosynthesis. In particular, a MnCa-oxo cluster contained into the photosystem II (PSII) protein promotes the water splitting to molecular oxygen, protons, and “energized” electrons; the latter ones are used for carbon dioxide reduction and chemical energy storage (e.g., sugar formation).<sup>1–4</sup> A technologically relevant approach to the solar-to-chemical energy-conversion process is referred to as artificial photosynthesis, which aims to emulate natural processes using man-made materials. The ultimate goal of artificial photosynthesis is to develop simplified “artificial leaves” that can be exploited for large scale generation of chemical fuels (e.g., hydrogen) directly from sunlight.<sup>5–10</sup> In this framework, the step involving water oxidation is considered to be a main bottleneck, hampering progress in the develop-

ment of applicable technologies. Several transition metal (TM)-based catalysts for such a process, containing different metal-oxo cores, in a close similarity with PSII, have been recently proposed.<sup>11–16</sup> Research into the archetypal biological process of photosynthetic water oxidation has also recently intensified, as it can serve as an important inspiration for the development of artificial water-splitting catalysts.<sup>12,17–19</sup> A full understanding of the structural properties of the whole class of water-splitting systems and, in turn, of the close relationship between characteristic motifs and catalytic mechanisms is considered as one of the main achievements of such investigations. A deeper insight into the transfer and localization of charge, with the ability to induce interfacial redox processes in complex environments, can provide new ideas for modified and improved catalysts. Such a quest for in-depth information is hindered by the often amorphous character of the oxide-(hydroxide) materials that have been recently the objects of

Received: May 19, 2015

Published: July 30, 2015



**Figure 1.** Idealized stick-and-ball models of the Mn-oxo amorphous catalyst. Several features are highlighted in the large panel A and shown as side-views in the panels B–E. In detail, a planar Mn-oxo sheet is liven up by (1) Mn vacancies, (2) out of plane  $\text{MnO}_6$  placed on top of a Mn vacancy, (3) out of plane  $\text{MnO}_6$  closing a complete cubane-like unit, (4) complete cubane-like unit acting as cross-linker between Mn-oxo sheets, (5) protonated  $\mu_2$ -OH bridges, (6) terminal Mn–OH and Mn–OH<sub>2</sub> species, and also forming (7) stable H–O–H...O–H structures. The lower panel illustrates the cross-linking role played by Mn adatoms (2,3) and cubane units (4).

wide discussion as water oxidation catalysts. The noncrystalline structure of these materials largely excludes insight in the atomic structure by conventional X-ray diffraction techniques. Therefore, the main source of atomic-level structural information is X-ray absorption spectroscopy (XAS), which is not limited by the need for crystalline order. However, the thereby accessible information is insufficient: the XAS spectra can facilitate determination of precise values of key distances but do not result in complete 3D models of atomic structure, protonation patterns, and oxidation-state localization. Structural models derived from X-ray absorption fine structure (XAFS) data are typically obtained by comparison with crystalline reference compounds which, however, may not contain all the mechanically crucial structural units of the amorphous material.

Among other TM-based catalysts, Mn-oxo compounds attract special interest because of several key features: unlike Ru or Ir, Mn is an earth-abundant first-row TM; unlike Co or Ni, it is nontoxic and fully biocompatible; unlike Fe, Zn, or Ti, the same Mn-oxo cluster has been selected by evolution to catalyze the water oxidation process in all the photosynthetic living organisms.<sup>20</sup> Not surprisingly, therefore, several new Mn-oxo catalysts for water oxidation, containing sometimes small amounts of Ca in order to maximize the similarities with PSII, have been recently synthesized.<sup>14,21–27</sup> Here we focus on one of these amorphous Mn oxides (hereafter referred to as MnCat), electrodeposited by oxidizing a  $\text{Mn}^{2+}$  aqueous solution.<sup>14</sup> Depending on the external potential applied to the starting solution, a full range of active to relatively inactive catalyst films has been obtained. A first structural characterization of the films included a series of XAS measurements, well suited for the

investigation of amorphous or poorly crystalline Mn-oxo compounds.<sup>28,29</sup> In particular, Mn K-edge XAS measurements<sup>14,23</sup> revealed that (i) inactive and active catalyst films are both formed by interconnection of an admixture of Mn(III)O<sub>6</sub> and Mn(IV)O<sub>6</sub> octahedra, possibly containing a small amount of residual Mn(II) ions; (ii) low-oxidation-state Mn ions are more abundant in the active film, up to 50% Mn(III) (a formal oxidation state of 3.5); and (iii) inactive films are more ordered than active films and similar to stable layered Mn oxides like lithiophorite, birnessite, and Ca<sub>2</sub>Mn<sub>3</sub>O<sub>8</sub>, well characterized by X-ray diffraction, scattering, and absorption measurements.<sup>22,30–33</sup>

On the grounds of such results, the MnCat has been viewed as a nanosized stacking of layered sheets formed by MnO<sub>6</sub> octahedra, cross-linked through defects.<sup>14,34</sup> An idealized model structure of MnCat is shown in Figure 1, where, in particular, several defects and characteristic motifs which can be found in the otherwise planar MnO<sub>6</sub> sheets are highlighted. Mn vacancies (1 in the Figure 1) are in-plane defects which can also host out-of-plane Mn atoms (2 in the Figure 1), holding the same position of Ca ions in the case of Ca<sub>2</sub>Mn<sub>3</sub>O<sub>8</sub>. Mn adatoms have been also suggested to stick on the sheet by forming local cubane-like configurations (3 in the Figure 1). The same cubane-like configurations, similar to that found in the case of PSII and involving one Ca atom, may act as efficient 3D cross-linkers when placed between two sheets (4 in the Figure 1).

The significance of these structural motifs for the catalytic function of the Mn oxides so far remained unclear and could not be verified based on extended X-ray absorption fine structure (EXAFS) simulations only. On the contrary, the close comparison between the results of ab initio calculations and XAS measurements is able to reveal at the atomistic scale the complex network of small metal-oxo units that usually aggregate to form catalytically active, amorphous oxides. Recent investigations of a prototypical electrodeposited amorphous cobalt-oxo film (CoCat), active as oxygen evolution catalyst,<sup>6</sup> showed indeed that highly refined XAS measurements of Co K-edge,<sup>35–37</sup> in combination with the results of ab initio calculations,<sup>38,39</sup> are able to pinpoint Co oxidation states and structural motifs. Once validated, such structures can be used to perform mechanistic studies which shed light on the formation of O–O bonds and on the oxidation states of reactive centers during the oxygen evolution process promoted by the catalyst.<sup>40–42</sup> Moreover, previous simulations of the CoCat structure<sup>38</sup> evidenced the role of two motifs involving O atoms placed at the boundaries of the catalyst: (i) protonated  $\mu_2$ -OH sites (5 in the Figure 1) induce longer Co–O distances than nonprotonated  $\mu_3$ -O sites. The difference was appreciable by refined EXAFS measurements in the case of the CoCat; (ii) Mn–Mn nearest neighbors carrying pairs of parallel Mn–O bonds are expected to form stable H–O–H···O–H structures (7 in the Figure 1) characterized by low-barrier H bonds.

Herein, we have performed a joint theoretical–experimental investigation of the properties of the MnCat active and inactive films, based on ab initio calculations and refined XAS analyses. The following discussion of our results has been organized in order to illustrate the close relationship between XAS and DFT findings. In detail, XAS measurements performed at the fully relaxed resting states of the catalyst films have been analyzed by using simplified guesses to produce EXAFS results. Such measurements and fits are discussed in Section 3.1 and compared with those previously obtained in the case of

partially oxidized films.<sup>14</sup> On the grounds of such results we have performed extensive theoretical simulations of several Mn-oxo clusters having atomistic structures compatible with EXAFS data obtained for the active and inactive films. We discuss first the correspondence between cluster models and subunits of known crystalline compounds (Section 3.2). We propose then an analysis of the first shell (Mn–O distances, Section 3.3) and of outer shells (Mn–Mn distances, Section 3.4). The quality and accuracy of our DFT-derived atomic distances have, in turn, stimulated and driven refined multishell analyses of the XAS measurements, which are discussed in Section 3.5. The overall results of such a positive-feedback mechanism are characterized by a finely tuned convergence between simulated structures and measurements. As a main result of our investigation, refined fits of XAS measurements are sizeably closer to experiment than simplified ones. We also provide an accurate and reliable characterization of the building units of the amorphous MnCat and of the protonation of  $\mu$ -oxo and terminal sites, together with insight into the local properties of Mn(II) and Mn(III) centers, which represent a distinctive fingerprint of the active film.

## 2. METHODS

MnCat models have been designed by using a wide collection of H-saturated Mn–O clusters, ranging from 6 to 20 Mn atoms, in order to test all the structures and motifs introduced in Figure 1. Such a setup has been proven to provide an accurate description of the structural and catalytic properties of amorphous oxides like the CoCat, as discussed in previous contributions.<sup>38,39,41</sup> Several constraints have driven the building of the investigated clusters: (i) XAS measurements suggested that (almost) all the Mn atoms are surrounded by six O atoms.<sup>14,22,23</sup> This implies the occurrence of several terminal O atoms (6 in Figure 1) at the MnCat/water interface. Terminal Mn–O species, as well as Mn–OH<sub>3</sub> ones, are expected to be unstable in resting conditions of the catalyst. The former has been supposed to be first intermediate of the O–O bond formation in Ca-assisted oxygen evolution<sup>2,22</sup> and to be formed only when the catalyst is exposed at high positive potential. The latter has been neither observed nor suggested by previous theoretical calculations of TM-oxo/water interfaces. Mn–OH and Mn–OH<sub>2</sub> species have been therefore considered to be present at the catalyst boundaries, with a particular attention to the optimal distribution of the stable H–O–H···O–H motifs mentioned above. (ii) H atoms play actually a role in the saturation of the MnCat, as confirmed by the fact that active catalysts can be also obtained from a starting solution containing Cl<sup>−</sup> or NO<sup>3−</sup> only as counterions of Mn(II), unable to act as ligand at the catalyst boundaries.<sup>14</sup> This is not a prerogative of Mn-based catalysts: CoCat active films have been obtained by using similar starting solutions containing Co(II) together with K<sup>+</sup> and Cl<sup>−</sup> counterions.<sup>43</sup> (iii) The total number of H atoms which saturate the cluster boundaries has been first chosen to ensure a Mn(IV) oxidation state, indicated as the resting state of the majority of Mn atoms in the inactive film by XANES measurements.<sup>14,23</sup> Further H atoms (one proton and one electron), or further electrons only, have been added to Mn(IV)-oxo clusters in order to obtain catalyst models containing up to 50% of Mn(III) sites, in agreement with the same XANES measurements of the active catalyst film. We note that Mn–Mn distances calculated in the case of isoelectronic clusters having different saturation patterns do not depend (within reasonable limits) on the total number of H atoms.

All of the MnCat models have been investigated by using ab initio simulations based on the Hubbard-U-corrected density functional theory (DFT+U) in an unrestricted open-shell Kohn–Sham framework, as implemented in the Quantum ESPRESSO suite of programs.<sup>44</sup> The H-saturated clusters have been accommodated into large periodic cubic supercells and fully optimized, until the forces on all nuclei were smaller than 0.001 au (Rydberg/Bohr) and until an

energy difference smaller than 0.0001 Ry was calculated between two steps of the minimization algorithm. The simulations have been carried out by using the  $\Gamma$ -point for the  $k$ -point sampling of the Brillouin zone, Kresse–Joubert PAW pseudopotentials<sup>45</sup> with non-linear core correction<sup>46</sup> taken from the Quantum-ESPRESSO pslibrary<sup>47</sup> and the U-corrected PBE exchange–correlation functional.<sup>48</sup> Kohn–Sham orbitals have been expanded into plane waves up to energy cutoffs of 60 and 360 Ry for the wave functions and the charge density, respectively, in order to achieve satisfactorily converged results. Such very strict convergence criteria on the plane wave basis set, as well as the inclusion of the Mn semicore 3s and 3p shells among the valence electrons, have proven to be necessary in order to estimate with high accuracy interatomic distances. A Hubbard U correction has been applied to the Hamiltonian. Such an approach has been already successful in improving the DFT description of electron correlation in TM oxides and related compounds, in particular when the localization of charge carriers (electrons and holes) is involved.<sup>41,49–53</sup> This is also particularly relevant in the case of mixed-valence oxides like the present MnCat, hosting Mn(II), Mn(III) and Mn(IV) ions, where the unpaired electrons localized at Mn centers must be carefully treated beyond the conventional local or semilocal approximations of the density functional.<sup>53,54</sup> In detail, a U correction for the 3d electrons of Mn atoms was set to the value of 3.9 eV, calculated in the case of several Mn(IV)O<sub>6</sub> centers belonging to different models by using the self-consistent linear response approach described in refs 49 and 55. A slightly lower value (3.5 eV) has been calculated in the same way in the case of Mn(III)O<sub>6</sub> centers. Such a small difference does not affect the structural properties of such centers. All the simulations have been therefore performed by using the former value for all the Mn atoms of all the clusters. In addition to the Mn 3d correction, a Hubbard U correction was applied also to the 2p electrons belonging to O atoms, since Coulomb interactions between p electrons of the oxo-ligands have to be considered comparable to those acting between the d electrons of the metals.<sup>56,57</sup> The strong coupling between Mn 3d and O 2p shells can indeed induce a spurious charge transfer from O atoms to Mn atoms when the U correction is applied to the metal d shell only.<sup>52</sup> For O atoms a U value of 5.9 eV has been applied by founding on experimental results, as detailed elsewhere.<sup>41,56,52</sup> Our DFT+U setup has been successfully tested against the structural properties of well investigated crystalline compounds like Pyrolusite MnO<sub>2</sub> and layered Ca<sub>2</sub>Mn<sub>3</sub>O<sub>8</sub>. The results are discussed in the [Supporting Information](#).

Regarding the unpaired electrons localized at Mn sites, it has to be also noted that exact-exchange corrections to semilocal functionals, as in the case of the popular B3LYP approach,<sup>58,59</sup> do not necessarily represent a good choice in the case of such strongly correlated open-shell systems. This is due to the static correlation error, which comes together with the Hartree–Fock exact-exchange contribution in hybrid functionals, leading to the overcoupling of unpaired electrons.<sup>60,61</sup> In order to provide a comparison of our DFT+U results, we have therefore selected a well-represented subset of the investigated clusters to perform a parallel B3LYP study. This second batch of calculations has been carried out by using the ORCA suite of programs<sup>62</sup> in a localized-basis-set framework. In detail, the Kohn–Sham orbitals have been expanded on a def2-TZVP Gaussian-type basis set.<sup>63,64</sup> The same def2-TZVP basis has been also used as an auxiliary basis set for Coulomb fitting. The 1s, 2s, and 2p Mn core electrons and 1s O core electrons have been replaced by Stuttgart–Dresden effective-core potentials (ECP) to ensure a close similarity between DFT+U and B3LYP calculations.<sup>65</sup> The achieved results are in a generally close agreement with those obtained at the DFT+U level of theory and are therefore reported in the [Supporting Information](#) for comparison.

MnCat active and inactive films were prepared by electrodeposition in aqueous solution of 0.5 mM Mn<sup>2+</sup> ions (0.5 mM Mn(CH<sub>3</sub>COO)<sub>2</sub>) using potential cycling or constant potential protocols as described in ref 14. The oxide films were then kept in Mn<sup>2+</sup>-free 0.1 M phosphate buffer for 30 min without application of an external potential. After this equilibration period the films were quickly frozen with liquid nitrogen without taking them out of the electrolyte and exposing them to air in order to preserve the relaxed state structure. The frozen films

were transferred to the liquid helium cryostat (Oxford) where the Mn K-edge XAS was measured at 20 K. The XAS measurements were performed at the Helmholtz-Zentrum Berlin für Materialien und Energie (formerly BESSY II, Berlin). The measurements at the manganese K-edge were acquired in fluorescence mode at the KMC-1 bending-magnet beamline using a 13 element ultralow energy resolving Ge detector (Canberra). The  $k^3$ -weighted EXAFS spectra in the range from 2.1 to 16.3 Å<sup>-1</sup> were simulated by least-squares curve fitting using the in-house software SimX3. The following EXAFS equation was used:<sup>66,67</sup>

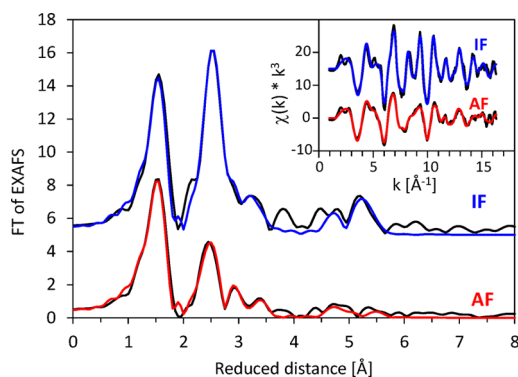
$$\chi(k) = S_0^2 \cdot \sum_i^{n_{\text{shell}}} \mathcal{R} \cdot \frac{N_i \text{Feff}_i}{k R_i^2} \cdot \exp(-2R_i/\lambda_i) \cdot \sin(2k \cdot R_i + \phi_{\text{eff}_i} + \phi_i) \cdot \exp(-2\sigma_i^2 \cdot k^2)$$

where the sum goes over the atomic shells (groups of elements with the same atomic number and similar distances from the X-ray absorbing atom),  $S_0^2$  is the amplitude reduction factor,  $\mathcal{R}$  is the total central atom loss factor,  $\text{Feff}$  is the effective curved-wave backscattering amplitude,  $N_i$  is the number of neighbors in the  $i^{\text{th}}$  atomic shell,  $R_i$  is the distance between the X-ray absorbing Mn atom and the atoms in the  $i^{\text{th}}$  atomic shell (backscatterer),  $\lambda$  is the mean free path in Å,  $\phi_{\text{eff}}$  is the phase shift for each shell,  $\phi$  is the total central atom phase shift, and  $\sigma_i$  is the Debye–Waller parameter of the  $i^{\text{th}}$  atomic shell (variation of distances around the average  $R_i$ ). The functions  $\mathcal{R}$ ,  $\text{Feff}$ ,  $\lambda$ ,  $\phi_{\text{eff}}$ , and  $\phi$  were calculated by Feff-8.4 (self-consistent field option activated).<sup>67,68</sup> The amplitude reduction factor  $S_0^2$  was set to 0.7. Additional details for the experimental data collection and EXAFS simulations are given in ref 22.

### 3. RESULTS AND DISCUSSION

**3.1. Simplified EXAFS simulations.** Details of the synthesis and of the XAS measurements of both MnCat active and inactive films were reported elsewhere.<sup>14</sup> As opposed to previous XAS analyses, the present results have been obtained by processing a different batch of measurements collected on the relaxed states of the MnCat films. In detail, the previously reported spectra<sup>14</sup> were taken after exposure of the films for 3 min at oxidizing potential, i.e., they do not reflect the resting state of the materials. In this work we analyze spectra taken after 30 min incubation of the electrodeposited films in a Mn<sup>2+</sup>-free 0.1 M phosphate buffer with no potential applied, in order to ensure that the structure is fully relaxed (as seen from the reached constant values for the open circuit potential). In this case the average oxidation state of Mn in both materials, as determined from the edge energy position, is lower than +4 (3.6 for the active catalyst and 3.7 for the inactive catalyst), i.e., the abundance of Mn(III) is higher (see [Figure S1](#)). As a first step of the analysis of these new EXAFS spectra we applied a simulation approach similar to that used in a previous investigation of similar amorphous layered oxides to the active and inactive catalyst films.<sup>34</sup> The results are shown in [Figure 2](#). Details of the fit parameters are reported in [Table S1](#).

Previous EXAFS analyses of electrodeposited Mn oxides where only one oxygen shell was included<sup>14</sup> indicated almost full 6-fold coordination for the inactive film, while a lower value, almost approaching a 5-fold coordination (5.3), was found for the active catalyst. The lower than 6 coordination number for the active catalyst was interpreted as an artifact of the employed simulation approach, in which only one oxygen shell was used to simulate two Mn–O distances corresponding to the presence of both Mn(III) and Mn(IV) ions in the structure of the catalyst. The coordination number obtained when a single Mn–O shell is considered in the new simulations is even lower (4.6 and 4.8 for the active and inactive films,



**Figure 2.** Fourier transformed EXAFS spectra for the active (AF) and inactive (IF) MnCat films. The original EXAFS spectra are shown in the inset. The experimental data are shown in black and the simulated spectra in color. Simulation parameters are given in Table S1 (simpler simulation approach).

respectively, as shown in Table 1), due to the greater abundance of Mn(III) in the relaxed structures. The fit of active catalyst with two shells with different Mn–O distances and common Debye–Waller factor for both shells yields an increased sum of two coordination numbers  $5.4 \pm 0.5$  (4.8 vectors at 1.89 Å and 0.6 vectors at 2.29 Å). For the inactive film the resulting coordination number is  $6.6 \pm 0.8$  (5.1 vectors at 1.90 Å and 1.5 vectors at 2.35 Å). This provides a hint that at least in the inactive film all Mn ions are likely 6-fold-coordinated but EXAFS alone is insufficient to elucidate further details.

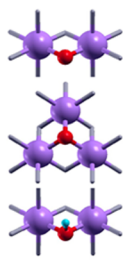

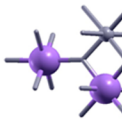


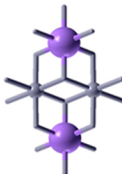
In addition to the oxygen shell we included in the simulation all the Mn–Mn shells identified previously for Mn-oxide powders.<sup>34</sup> The fit parameters and simulated curves are shown in Table 1 and in the SI. The overall distances agree very well with a layered structure with different degrees of disorder for the active and for the inactive films. However, these results alone cannot provide a complete 3D atomistic picture of the oxide film structures and motifs. Increasing of the number of shells without adding complementary information would also result in data overparametrization and, in turn, in an unstable fit. For these reasons we have performed an extensive DFT-based study of several model clusters of MnCat, whose results are discussed in the following Sections. Combining EXAFS results with such DFT calculations, we aim at reaching a better description of the structure of the active and inactive oxides which can guide the analysis of XAS data fitted with more shells. Starting values for the distances of these new shells come from the results of DFT calculations. In addition, as protons are invisible by EXAFS spectroscopy, the protonation state of the bridging and terminal oxygen atoms can be indirectly derived from the comparison between Mn–O and Mn–Mn distances found by DFT calculation and the same distances obtained by EXAFS simulations.

**3.2. Structural Models Considered in DFT Calculations.** The results from the first EXAFS simulations indicate that the MnCat is likely formed by small, ordered units interconnected to form still unknown patterns.<sup>14,23</sup> To elucidate further structural details, we have performed DFT calculations focusing on five H-saturated Mn-oxo clusters, shown in Figure 3, in order to compare their structural properties (e.g., Mn–Mn and Mn–O distances) with previous experimental findings. Our models contain all the atomistic motifs introduced above and summarized in Figure 1: the first cluster (A in Figure 3) is cut out from a two-dimensional sheet

formed by MnO octahedra arranged in a hexagonal lattice. Such kind of planar lattice is often referred to as brucite structure (from the structure of  $\text{Mg}(\text{OH})_2$ ) and is commonly found in layered TM oxides like, e.g.,  $\text{LiCoO}_2$ , Heterogenite  $\text{CoO}(\text{OH})$ , several Mn-based birnessites and also Ni hydroxides.<sup>8,38,69–74</sup> A second cluster (B in Figure 3), cut out from the Mn-birnessite structure, is characterized by a Mn vacancy in the two-dimensional sheet surmounted by an out-of-plane  $\text{MnO}_6$  group. In a third cluster (C in Figure 3) the same out-of-plane  $\text{MnO}_6$  group is placed on the top of the A cluster to close a complete  $\text{Mn}_4\text{O}_4$  cubane-like unit. A fourth cluster (D in Figure 3) is cut out from the  $\text{Ca}_2\text{Mn}_3\text{O}_8$  structure, another synthetic layered Mn oxide,<sup>30</sup> by replacing the Ca atom, sandwiched between two Mn-oxo layers with a further Mn atom. A final cluster (E in Figure 3) is formed by two B clusters sharing the same Mn atom. Such a subset has been chosen among a large number of investigated models, formed by 6–20  $\text{MnO}_6$  octahedra, in order to illustrate the one-to-one correspondence found between all the calculated and measured Mn–Mn and Mn–O distances. A complete summary of all of the investigated systems, useful to assess the reliability of our theoretical model, but redundant to the purposes of our study, is given in the Supporting Information

**3.3. First Coordination Sphere: Mn–O Distances.** Mn–O bonds do not provide direct information about the extended structure of the catalyst, because the first Mn–O shell only is detectable with accuracy by XAS measurements. From the experimental results, a lower value, approaching a 5-fold coordination, is found in the case of the active catalyst. Even in the limit of the slight (1%) overestimation of Mn–O bonds calculated in the case of the Pyrolusite  $\text{MnO}_2$  and layered  $\text{Ca}_2\text{Mn}_3\text{O}_8$  (see Supporting Information), the values calculated in the case of the B–E clusters are definitely larger when the average oxidation state of Mn atoms is lower than 4.0. This is mainly due to the electronic properties of Mn(III) $\text{O}_6$  centers (sketched in Figure 4f), characterized by a significant Jahn–Teller (JT) distortion induced in the d4 Mn(III) site by the strong octahedral field of the oxo ligands.<sup>75,76</sup> The JT distortion of Mn(III) induces the elongation of two opposite Mn–O bonds with different effects depending on the nature of the involved O atoms: in the case of  $\mu_2$ -O and  $\mu_3$ -O oxo bridges (sketched in Figure 4a,c, respectively, and represented by red spheres in Figure 3), as well as of terminal Mn–OH species (Figure 4d, yellow spheres in Figure 3), the Mn–O bonds are stretched from a 1.9 Å value to a 2.1–2.2 Å value. In the case of terminal Mn–OH<sub>2</sub> species (Figure 4e, green spheres in Figure 3), the water molecules go farther (Mn–O distance larger than 2.3 Å) and cannot be considered anymore as bonded to Mn, in agreement with the suggestion of undercoordinated Mn(III) sites in the active catalyst, where Mn has a lower average oxidation state. A second effect contributes to a lesser extent to the modulation of the Mn–O distance. As already observed in the case of the CoCat,<sup>38</sup> and also suggested in the case of PSII,<sup>19</sup>  $\mu_2$ -O sites are eligible sites for protonation. Protonated  $\mu_2$ -OH sites in the MnCat models (Figure 4b, blue spheres in Figure 3) are characterized by slightly elongated Mn–O bonds (1.95 Å). The presence of residual Mn(II) in the MnCat could not be excluded on the grounds of XANES measurements.<sup>23</sup> Despite of several different starting distributions of charge and spin on Mn atoms attempted on all the clusters, there is only one of the investigated sites where a Mn(II) ion is stable, namely the Mn atom sandwiched between two sheets in the E cluster (see Figure 3). Such a site is surrounded by six

Table 1. Structural Properties of the A–E Clusters Shown in Figure 3 at Different Average Mn Oxidation States<sup>a</sup>

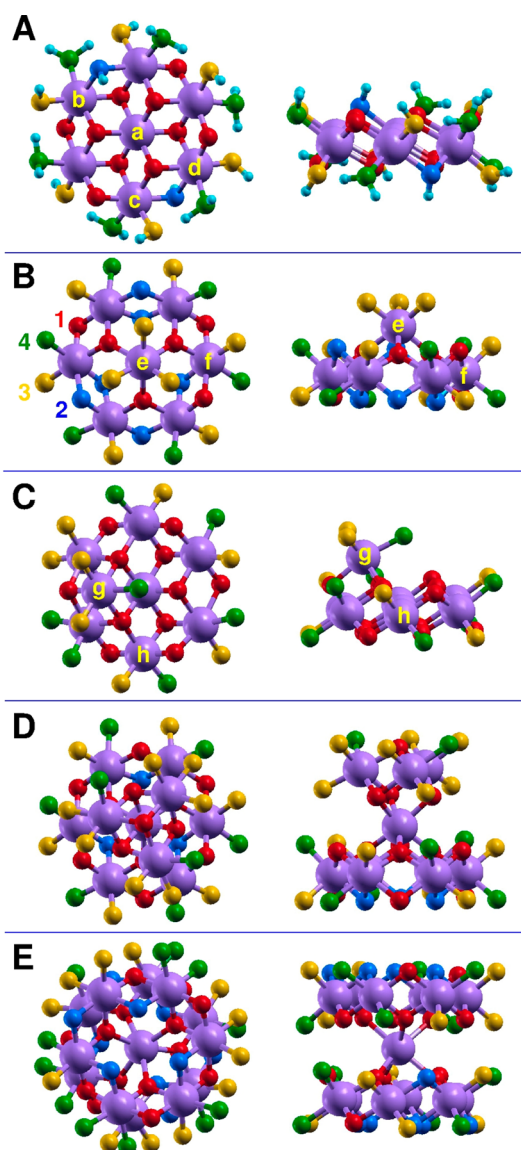
Cluster (Mn Ox. State)	Bond Distance (Å)					
	Mn-O	Mn-Mn 1	Mn-Mn 2	Mn-Mn 2*	Mn-Mn 3	Mn-Mn 4
						
<b>A (4.00)</b>	1.91 (0.06)	2.88 (0.06)	-	-	4.99 (0.04)	5.77 (0.01)
<b>B (4.00)</b>	1.91 (0.07)	2.86 (0.06)	3.52 (0.04)	-	4.96 (0.05)	5.73 (0.01)
<b>B (3.86)</b>	1.92 (0.07)	2.86 (0.06)	3.53 (0.05)	-	4.96 (0.06)	5.73 (0.05)
<b>B (3.71)</b>	1.93 (0.07)	2.89 (0.08)	3.53 (0.07)	-	5.00 (0.11)	5.77 (0.14)
<b>B (3.57)</b>	1.95 (0.09)	2.93 (0.10)	3.51 (0.08)	-	5.07 (0.14)	5.85 (0.17)
<b>C (4.00)</b>	1.93 (0.07)	2.93 (0.07)	-	4.20 (0.19)	5.05 (0.13)	5.86 (0.11)
<b>C (3.75)</b>	1.94 (0.08)	2.95 (0.08)	-	4.19 (0.22)	5.08 (0.13)	5.89 (0.12)
<b>C (3.50)</b>	1.98 (0.12)	2.99 (0.08)	-	4.14 (0.09)	5.15 (0.12)	5.99 (0.08)
<b>D (4.00)</b>	1.92 (0.06)	2.90 (0.07)	3.48 (0.04)	-	4.93 (0.19)	5.99 (0.25)
<b>D (3.80)</b>	1.94 (0.11)	2.93 (0.11)	3.52 (0.07)	-	5.02 (0.17)	6.06 (0.32)
<b>D (3.60)</b>	1.96 (0.11)	2.96 (0.11)	3.52 (0.11)	-	5.00 (0.20)	6.05 (0.27)
<b>E (3.85)</b>	1.93 (0.10)	2.86 (0.06)	3.65 (0.05)	-	4.89 (0.17)	5.75 (0.07)
<b>E (3.69)</b>	1.94 (0.11)	2.88 (0.07)	3.66 (0.08)	-	4.89 (0.17)	5.79 (0.13)
<b>E (3.54)</b>	1.97 (0.13)	2.91 (0.08)	3.70 (0.13)	-	4.93 (0.19)	5.82 (0.17)
	<i>MnCat XAS Data</i>					
<b>Inactive Film</b>	1.90 [4.8]	2.88 [6.7] 3.13 [1.8]	3.53 [2.3] 3.75 [0.7]		5.05 [2.2]	5.55 [4.6] 5.75 [0.7]
<b>Active Film</b>	1.89 [4.6]	2.89 [5.0] 3.12 [1.5]	3.48 [0.6] 3.79 [0.6]		5.05 [1.1]	5.42 [1.1] 5.77 [0.3]

<sup>a</sup>The Mn–O column is related only to distances between Mn atoms and oxo bridges. Mn–O distances involving terminal O atoms are discussed in Section 3.5. Mn–Mn 1, 2/2\*, 3, and 4 columns are related to nearest-neighbor, next-nearest-neighbors, etc., distances, as sketched in the small insets placed at the column headers. Mn–Mn 2 and 2\* distances are related to the presence of different kinds of out-of-plane Mn atom that cannot be found within the same cluster. They have been therefore grouped in different columns. Data have been averaged on different distances of the same type, and standard deviations ( $\sigma$ ) are reported in round brackets. XAS results shown in Figure 2 have been also summarized at the end of the table. Square brackets contain coordination numbers obtained by EXAFS simulations in the case of XAS data; further details can be found in the Supporting Information.

undistorted oxo ligands all having a planar structure, a motif not shared with any other Mn atom belonging to all the investigated clusters. Apart from the lack of distortion of the Mn(II) site, characterized by longer (2.17 Å) Mn–O distances than Mn(III) or Mn(IV), our finding is also supported by a detailed Bader's charge analysis of the E cluster reported in the Supporting Information. It is shown there that Mn(II), Mn(III), and Mn(IV) species can coexist within the same cluster, as also observed in the case of synthetic polynuclear Mn complexes.<sup>77,78</sup> We note that the Mn(II)–O contribution to the Mn–O shell cannot be resolved by EXAFS, because it is masked by the more abundant Mn(III)–O ones falling in the same range. However, as opposed to Mn(III)O<sub>6</sub>, Mn(II)O<sub>6</sub>

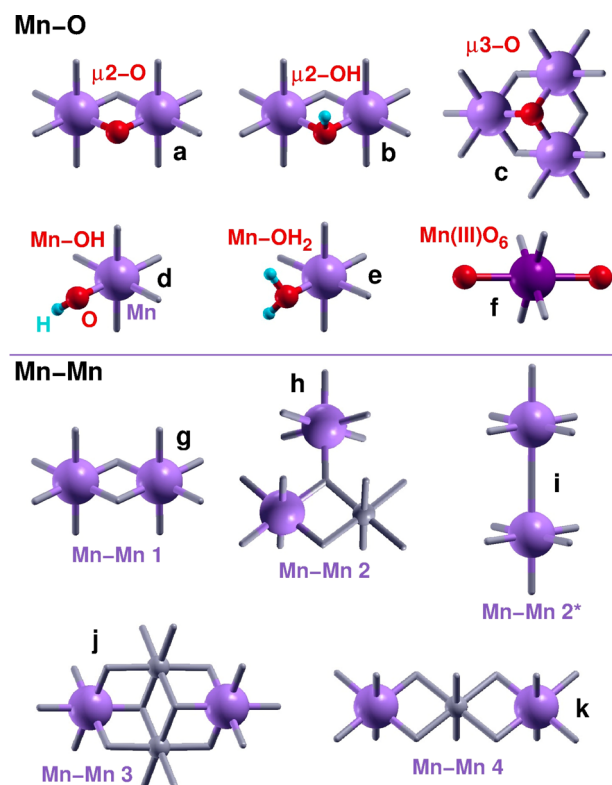
octahedra are isotropically larger than Mn(IV)O<sub>6</sub>, and their occurrence is indirectly confirmed by a characteristic elongation of the corresponding Mn–Mn 2 shell detected by EXAFS, as discussed in the following Section 3.4. A detailed, quantitative evaluation of the occurrence of different Mn–O bonds, together with their assignment to the different O-related species, is discussed below in Section 3.5.

**3.4. Short-Range Mn–Mn Distances.** As opposite to Mn–O distances, Mn–Mn short-range distances are more directly connected to the atomistic texture of MnCat. However, the modulation of Mn–O distances discussed above is responsible for the partition of Mn–Mn shells in subshells, connected, in turn, to characteristic fingerprints of the MnCat



**Figure 3.** Sticks-and-balls models of Mn(IV)-oxo H-saturated clusters. (A)  $\text{Mn}_7\text{O}_{24}\text{H}_{20}$  flat cluster cut out from a birnessite-like sheet. Different kinds of O atoms are represented by using different colors: red ( $\mu_2$ -O and  $\mu_3$ -O oxo bridges); blue (protonated  $\mu_2$ -OH oxo bridges); yellow (terminal Mn-OH groups); green (terminal Mn-OH<sub>2</sub> groups). The same colors are used for the other models, even if H atoms are not shown in the B-D parts for the sake of clarity. (B)  $\text{Mn}_7\text{O}_{27}\text{H}_{26}$  cluster cut out from a birnessite-like sheet including one Mn adatom placed above a Mn vacancy. (C)  $\text{Mn}_8\text{O}_{27}\text{H}_{22}$  cluster formed by adding to the A cluster one out-of-plane Mn atom which completes a cubane-like Mn-oxo unit. (D)  $\text{Mn}_{10}\text{O}_{37}\text{H}_{34}$  cluster formed by building a complete cubane-like Mn-oxo unit around the out-of-plane Mn adatom of the B cluster. (E)  $\text{Mn}_{13}\text{O}_{48}\text{H}_{46}$  cluster formed by two B clusters sharing the same Mn adatom. The a-h labels identify Mn-Mn distances discussed in text and tables: a-b (Mn-Mn 1); e-f (Mn-Mn 2); g-h (Mn-Mn 2); b-c (Mn-Mn 3); b-d (Mn-Mn 4).

motifs. As discussed on the grounds of previous XAS results,<sup>14,22</sup> the measured Mn-Mn distances can be grouped in four well-separated shells. The corresponding calculated values are shown in Table 1 for all the systems discussed here<sup>79</sup> and are in a generally good agreement with the results of EXAFS analyses reported in the same table. We note that the first two shells (Mn-Mn 1 and 2 in the table) are characterized



**Figure 4.** Motifs which characterize the simulated MnCat structures and correspond to measured Mn-O (a-f) and Mn-Mn (g-k) distances are sketched in the figure as ball-and-stick models. The relevant Mn, O, and H atoms involved in the structures are shown as purple, red, and light-blue spheres. Further Mn (O) atoms not directly involved in the structures and distances are represented instead as gray small spheres and sticks (sticks only). The same labels have been used in all the tables to identify calculated and measured distances.

by narrow distributions of the calculated values, with standard deviations in substantial agreement with those estimated in the case of EXAFS simulations. On the other hand, the outer shells (Mn-Mn 3 and 4 in the table) can group qualitatively different Mn-Mn pairs, e.g., in-plane and plane-to-plane distances in the case of clusters D and E. This situation is compatible with the occurrence of DFT distances which are basically corresponding to measured ones, but with relative populations which are too strongly dependent on the cluster shape and on the lack of an extended network to yield representative statistical parameters. The planar A cluster already contains three of the four Mn-Mn measured shells, namely Mn-Mn 1 (2.9–3.1 Å, sketched in Figure 4g), Mn-Mn 3 (5.0–5.1 Å, Figure 4j), and Mn-Mn 4 (5.4–5.8 Å, Figure 4k) in Table 1. This can be considered as sound proof of a layered structure of the MnCat, characterized by Mn-oxo sheets cross-linked through defects. A further measured shell, Mn-Mn 2/2\* (3.5–3.8 Å, Figure 4h,i) in Table 1, appears only in the case of the remaining B–E clusters, containing out-of-plane Mn atoms or Mn-oxo structures, thus providing a first indication of the nature of such cross-linking defects. We can identify four of such structures, contained in the B–E models and corresponding to four different fingerprints of the measured spectra. The Mn adatom placed on the top of a Mn vacancy in the B cluster is responsible for the Mn-Mn 2 shell, peaked at 3.4–3.5 Å in the EXAFS spectra as well as for the 5.4–5.5 Å contribution to the Mn-Mn 4 shell, which can be only found in larger models discussed in the Supporting

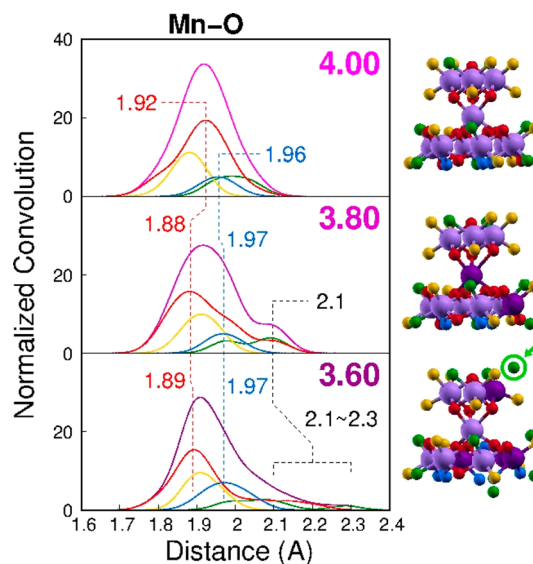
**Information.** A similar adatom placed closer to the sheet to form a complete cubane unit, as in the C cluster, can be related instead to the 2\* subshell ( $\sim 4.2$  Å), not resolved in previous EXAFS analyses. The D cluster contains the same Mn adatom of B, which is also the vertex of a complete cubane unit not in direct contact with the sheet, as opposed to that found in C. We can therefore distinguish the fingerprint of the adatom (same 3.4–3.5 Å values in D of the Mn–Mn 2 shell of B) from the fingerprint of the complete cubane unit (longer Mn–Mn 1 distance in C and D than in A, approaching the 3.1 Å subshell in the EXAFS spectra). Finally, the longer Mn–Mn 2 distance calculated in the case of E is the fingerprint of the Mn(II) atom placed between two sheets, corresponding to the 3.7–3.8 Å subshell in the EXAFS analysis.

When the average oxidation state of Mn is lowered by introducing Mn(III) ions in the models, the inherent, significant JT distortion of Mn(III)O<sub>6</sub> centers induces a progressive elongation of all the Mn–Mn distances. A similar elongation of most shells has been reported in the case of the active catalyst, as opposed to the inactive film (see Table 1), thus supporting the idea that a certain abundance of Mn(III) sites in a mixed Mn(III)–Mn(IV) architecture of the metal-oxo structure is a crucial feature of more active catalytic systems. An important finding in our study is that Mn(III) ions are always localized at the boundaries of all the models, even of larger ones (shown in the Supporting Information) where inner Mn atoms can be entirely surrounded by  $\mu_3$ -O oxo bridges. This is due to the fact that terminal O atoms, especially those belonging to Mn–OH<sub>2</sub> groups, can relax more easily than inner  $\mu_2$ -O and  $\mu_3$ -O bridges (compare the different structures in Figure 4). They drive, therefore, the JT distortion of Mn(III) sites. This implies also that when the active catalyst is exposed to a positive external potential to start the oxygen evolution reaction, electrons are easily drained from such Mn(III) sites in contact with the water solution, which are oxidized to Mn(IV): if we look at such process with a complementary point of view, the oxidizing holes injected in the catalyst are localized at the catalyst/water interface, where they can readily attack neighboring water molecules.

Finally, the presence of Mn(II) ions trapped between two parallel Mn-oxo sheets is univocally responsible for the 3.7–3.8 Å contribution to the Mn–Mn 2 shell, which is longer in the case of the E cluster than in all the other models irrespective of the presence of Mn(III). We note that there is no way to force such a special site to assume a Mn(III) or Mn(IV) character: for example, if all the Mn atoms of the E cluster are forced to assume a formal (IV) oxidation state, the Mn(II) drains charge from all of the neighbors to keep its very stable d<sup>5</sup> configuration. However, the unique position of Mn(II), protected from incoming water molecules, and its resistance to oxidation suggest that it is an unlikely player in oxygen evolution processes, even if it may have a structural role for the assembly and shaping of the amorphous catalyst.

**3.5. Refined EXAFS Modeling and Simulations.** The structural data collected in Table 1 and discussed in Sections 3.3 and 3.4 show a generally good agreement between EXAFS and ab initio results. However, non-negligible discrepancies indicate that there is still significant room for improvement of the theoretical model as well as of the fitting procedure of the XAS data. In order to fill in the most satisfactorily way all the remaining gaps between experiment and theory, we have first calculated a series of DFT-based EXAFS spectra on the grounds of the A–E structures calculated at the DFT+U level

of theory.<sup>80</sup> In detail, the simulated spectra have been obtained by convolution of Gaussian functions ( $\sigma = 0.0387$ ), centered on the calculated Mn–O (first shell only) and Mn–Mn distances and normalized to the number of Mn atoms belonging to the clusters. We have selected two case studies to illustrate the fine analysis of Mn–O and Mn–Mn distances at different values of the average Mn oxidation state: modeled EXAFS spectra of the first Mn–O shell belonging to the D cluster are shown in Figure 5, while those related to the first and second Mn–Mn

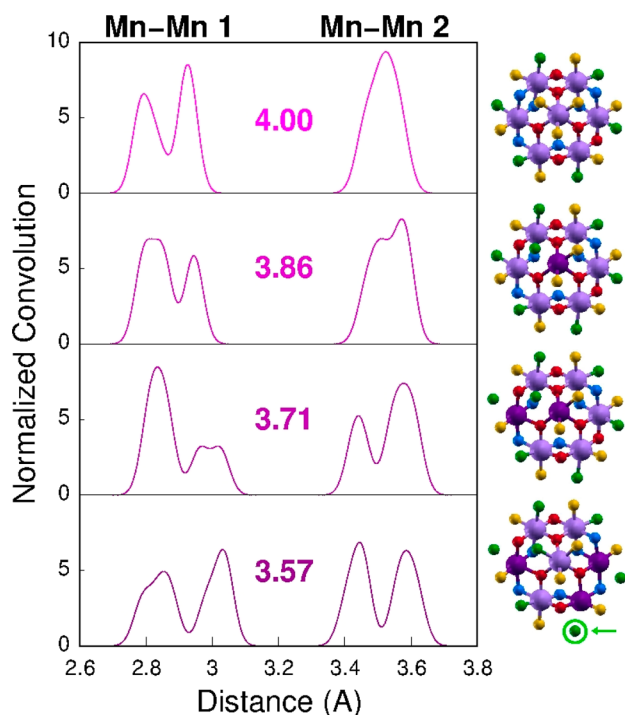


**Figure 5.** DFT-based EXAFS modeling of the first Mn–O shell of the D cluster. The plots are obtained by convolution of Gaussian functions ( $\sigma = 0.0387$ ), centered on the calculated Mn–O distances and normalized to the number of Mn atoms belonging to the cluster. The magenta plots are the sums of the red, blue, yellow, and green curves, representing the contributions of  $\mu_2$ -O and  $\mu_3$ -O species (red),  $\mu_2$ -OH species (blue), terminal Mn–OH species (yellow), and terminal Mn–OH<sub>2</sub> species (green). All the different kinds of Mn–O bond are also sketched in Figure 4. The average oxidation state of Mn is reported in each panel and corresponds to the distribution of Mn(IV) sites (light purple spheres) and Mn(III) sites (dark purple spheres) sketched in the models on the right-side. A green arrow indicates one of the terminal water molecules detached from Mn(III) due to the effect of a strong JT distortion.

shells of the B cluster are shown in Figure 6. All the results of similar calculations performed on the remaining structures are summarized in Table 2 (Mn–O distances) and Table 3 (Mn–Mn distances).

Let us focus first on Mn–O bonds. The DFT-modeled EXAFS spectra displayed in Figure 5 (magenta curves) can be separated in four different contributions, corresponding to the bonding of Mn with  $\mu_2$ -O and  $\mu_3$ -O species (red curves),  $\mu_2$ -OH species (blue curves), terminal Mn–OH groups (yellow curves), and terminal Mn–OH<sub>2</sub> groups (green curves). All such species are also sketched in Figure 4a–e. We note that the usage of small size saturated clusters as models of the extended amorphous MnCat structure implies an overestimation of the amount of terminal groups, which should be largely replaced by further oxo bridges connecting the catalyst building blocks. On the other hand, terminal groups are necessarily present at the catalyst/water interface, because they ensure the 6-fold coordination of surface Mn sites, where they are likely to be primary characters in the oxygen evolution process, as





**Figure 6.** DFT-based EXAFS modeling of the first and second Mn–Mn shells of the B cluster. The plots are obtained by convolution of Gaussian functions ( $\sigma = 0.0387$ ), centered on the calculated Mn–Mn distances and normalized to the number of Mn atoms belonging to the cluster. The average oxidation state of Mn is reported in each panel and corresponds to the distribution of Mn(IV) sites (light-purple spheres) and Mn(III) sites (dark-purple spheres) sketched in the ball-and-stick models. A green arrow indicates one of the terminal water molecules detached from Mn(III) due to the effect of a strong JT distortion.

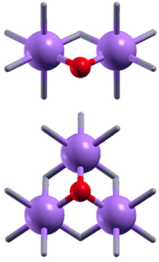
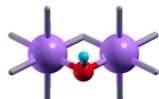
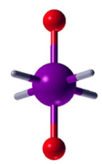
previously suggested in the case of CoCat.<sup>41,81</sup> We have therefore based our quantitative structural analysis of Mn–O distances mainly on the distribution of  $\mu$ -oxo bonds at different average Mn oxidation states, with some qualitative indications of the behavior of terminal Mn–OH and Mn–OH<sub>2</sub> groups. When all the Mn atoms are Mn(IV), the Mn–O peak is highly symmetric, broadened only by the separation between nonprotonated (red curve) and protonated (blue curve) oxo bridges. Mn(III) sites (two in the 3.80 panel, and four in the 3.60 panel) induce a prominent asymmetry on the right side of the peak. In detail, such a feature is mainly due to the elongation of Mn–OH<sub>2</sub> bonds, which is concomitant with the elongation of a corresponding amount of opposite Mn– $\mu_3$ -O bonds: the JT distortion of the Mn(III)O<sub>6</sub> octahedra preferentially involves such species in all the investigated clusters. When the average oxidation state of Mn approaches the value of 3.5 (see the 3.6 panel of Figure 5), a significant amount of disorder affects the red and green curves. The former curve displays a long tail on the right side which does not affect the position of its main peak, while the latter curve is almost entirely flattened: some of the water molecules are completely detached from Mn(III) sites, as also indicated by the green arrow in the figure, thus lowering the coordination number of Mn at the MnCat/water interface. We can therefore distinguish three different contributions to the Mn–O shell, identified by dashed lines in Figure 5: (i) a first subshell involving the undistorted  $\mu_2$ -O and  $\mu_3$ -O species (dashed red line); (ii) a second subshell involving protonated  $\mu_2$ -OH

species (dashed blue line); (iii) a third subshell, broader than the first two, involving the species undergoing the strong JT distortion related to Mn(III) sites, also masking the Mn(II)- $\mu_3$ -O distances found only in the case of the E cluster. All such contributions have been resolved in the new, more comprehensive analysis of the XAS data, with the corresponding values measured in the case of the active and inactive films reported in the last two lines of Table 2, together with the subshell theoretical analysis of all the other investigated clusters. Such new data are in striking agreement and confirm that our cluster models describe very accurately the coordination of Mn atoms in all the oxidation states, motifs, and local features of the amorphous MnCat.

In the case of Mn–Mn distances, a more detailed analysis involves the first and second Mn–Mn shells only (Figure 4g–i), because they already contain the fingerprints of all the structural motifs of MnCat and are also less affected by the particular choice of a given cluster model. The DFT-modeled EXAFS spectra of the B cluster at different Mn oxidation states, displayed in Figure 6, show very clearly that the subshell partitioning is even easier: the peaks are clearly split at the 0.0387 Å Gaussian broadening used to represent Mn–Mn distances, and they are characterized by a subshell patterning dependent on the Mn oxidation state. In detail, the presence of protonated  $\mu_2$ -OH species (blue spheres in the right insets to Figure 6) is responsible for a first splitting of the Mn–Mn 1 shell (1a and 1b in Table 3), observable in absence of Mn(III). As opposed to the B cluster, the A and C clusters, containing a lesser amount of protonated  $\mu_2$ -OH bridges in their higher Mn oxidation states, are characterized by unresolved Mn–Mn 1 shells, as reported in Table 3. This is a second fingerprint of the presence of protons on  $\mu_2$ -O bridges, also supporting the recent suggestion that similar protonated bridges could be present in the MnCa-oxo cluster of PSII.<sup>19</sup> The two subshells are broadened by the disorder that Mn(III) sites introduce in the structures, but they are still well resolved, as shown by the lower panels of Figure 6. A third subshell, peaked at 3.1 Å (1c in Table 3), appears only when complete cubane units hosting Mn(III) sites are present in the clusters (models C and D, see Figure 3) and represent therefore a fingerprint of such motifs. Once again, the partitioning of the Mn–Mn 1 shell suggested on the grounds of theoretical modeling drove the refined analysis of XAS data. The EXAFS results, obtained by using a three-subshell model, are reported at the end of Table 3 and show a very close agreement with the calculated distances.

The Mn–Mn 2 shell (distances longer than 3.4 Å) is strictly related to the presence of Mn adatoms not belonging to the planar backbone of the catalyst structure, which can occupy different positions above or between Mn-oxo sheets. No similar distance can be found within the planar sheets in any oxidation state of Mn atoms. Our theoretical results indicate that such different positions of Mn adatoms give rise to different Mn–Mn distances and that they are therefore responsible for the subshell partitioning on the Mn–Mn 2 shell as well as for the occurrence of clear fingerprints of specific motifs in the measured EXAFS. In the case of clusters B and D the Mn adatom is placed on the top of a Mn vacancy in the Mn-oxo sheet, and it is connected to its six nearest-neighbors Mn by three planar  $\mu_3$ -O bridges, never protonated in all of the ab initio simulations. This implies that the Mn–Mn 2 shell (3.4–3.8 Å) is not split when all the involved atoms are Mn(IV), as shown by the upper panel of Figure 6. A clear splitting of the shell in two contributions (2a and 2b in Table 3) is directly

Table 2. Mn–O Fine Comparison. Refined Analysis of Calculated and Measured Mn–O Distances<sup>a</sup>

Cluster (Mn Ox. State)	Bond Distance (Å)		
	Mn–O a	Mn–O b	Mn–O c
			
A (4.00)	1.90	1.97	-
B (4.00)	1.85	1.93	-
B (3.86)	1.86	1.95	2.05-2.25
B (3.71)	1.87	1.97	2.05-2.25
B (3.57)	1.87	1.99	2.05-2.25
C (4.00)	1.91	-	-
C (3.75)	1.92	1.99	2.2-2.4
C (3.50)	1.94	2.00	2.2-2.4
D (4.00)	1.92	1.96	-
D (3.80)	1.88	1.97	2.1
D (3.60)	1.89	1.97	2.1-2.3
E (3.85)	1.86	1.95	2.17 <sup>b</sup>
E (3.69)	1.87	1.97	2.05-2.25
E (3.54)	1.86	1.99	2.1-2.3
	<i>Refined XAS Data</i>		
Inactive Film	1.87 [2.7]	1.95 [2.3]	2.37 [1.2]
Active Film	1.85 [2.3]	1.94 [2.4]	2.28 [0.5]

<sup>a</sup>As detailed in the text, the Mn–O shell is partitioned in three subshells corresponding to (Mn–O a) non-protonated  $\mu_2$ -O and  $\mu_3$ -O bridges; (Mn–O b) protonated  $\mu_2$ -OH bridges; (Mn–O c) JT distorted Mn(III)–O bonds. Theoretical values are related to the A–E clusters discussed in the text, having different average oxidation states of the Mn atoms. Data have been averaged on different distances of the same type, and standard deviations ( $\sigma$ ) are reported in round brackets. XAS results shown in Figure 7 have been also summarized at the end of the table. Square brackets contain coordination numbers obtained by EXAFS simulations in the case of XAS data; further details can be found in the Supporting Information.

<sup>b</sup>Mn(II)–O distance.

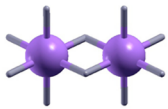
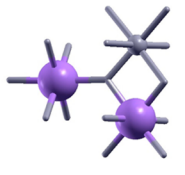
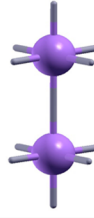
connected to the average oxidation state of Mn atoms, the lower the oxidation state, the deeper the separation between the peaks, whose relative populations depend on the localization of the Mn(III) sites. The same two subshells can be found in the case of the E cluster, but they are both shifted to longer distances because, as opposed to the B and D clusters, a Mn(II) atom is placed between the two Mn-oxo sheets, as discussed in the previous Section 3.3. Such a complex situation framed by theoretical results is in partial agreement with the refined EXAFS results reported at the end of Table 3. The 2a and 2b shells cannot be resolved by the analysis of XAS data and are therefore grouped in a single subshell at 3.5 Å, substantially falling in the middle of the calculated 2a and 2b data. A second subshell at 3.7–3.8 Å compares nicely with the Mn–Mn 2 distances calculated for the E cluster only and can be considered as a firm indication of the presence of a small amount of residual Mn(II) in the catalyst. The longer 4.2 Å distance (2c in Table 3) is found instead in both the calculated and the new measured data and corresponds to the linear “rocksalt-like” Mn–O–Mn chain, sketched in Figure 4i, that is

a distinctive feature of the cubane motif of cluster C, the only one embedded within the Mn-oxo sheet.

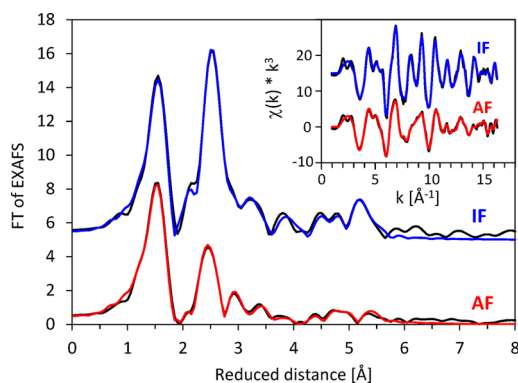
As a final remark, we note the significant improvement of the new EXAFS analysis of the catalyst films shown in Figure 7, driven by the ab initio results illustrated above. A comparison with the simplified fits reported in Figure 1 clearly indicates that multishell fits based on theoretical predictions of Mn–O and Mn–Mn distances yield a faithful representation of the XAS measurements.

**3.6. Comparison between the Structures of Active and Inactive Films.** On the grounds of the discussion of the measured and calculated Mn–Mn and Mn–O distances and of the corresponding structures and motifs, we can draw an atomistic identikit of the active and inactive films. We already knew from previous measurements<sup>14</sup> that inactive films were characterized by a larger connectivity network than catalytically more active samples. In agreement with such suggestion, the present ab initio simulations and the subsequent refined EXAFS results show that the Mn–Mn 1 shell is composed by three well-resolved subshells, substantially peaked at the same

Table 3. Mn–Mn Fine Comparison<sup>a</sup>

Cluster (Mn Ox. State)	Bond Distance (Å)					
	Mn–Mn 1a	Mn–Mn 1b	Mn–Mn 1c	Mn–Mn 2a	Mn–Mn 2b	Mn–Mn 2c
						
<b>A (4.00)</b>	2.88 (0.05)			-		
<b>B (4.00)</b>	2.80 (0.03)	2.93 (0.01)	-	3.52 (0.04)		-
<b>B (3.86)</b>	2.82 (0.03)	2.94 (0.01)	-	3.49 (0.03)	3.58 (0.01)	-
<b>B (3.71)</b>	2.84 (0.02)	2.99 (0.04)	-	3.44 (0.02)	3.58 (0.03)	-
<b>B (3.57)</b>	2.84 (0.04)	3.02 (0.03)	-	3.44 (0.02)	3.59 (0.03)	-
<b>C (4.00)</b>	2.91 (0.05)		3.06 (0.02)	-		4.20 (0.19)
<b>C (3.75)</b>	2.84 (0.01)	2.97 (0.05)	3.13 (0.01)	-		4.19 (0.22)
<b>C (3.50)</b>	2.83 (0.01)	2.97 (0.04)	3.10 (0.02)	-		4.18 (0.13)
<b>D (4.00)</b>	2.81 (0.01)	2.94 (0.03)	-	3.48 (0.04)		-
<b>D (3.80)</b>	2.85 (0.03)	2.96 (0.05)	3.14 (0.02)	3.42 (0.02)	3.57 (0.01)	-
<b>D (3.60)</b>	2.85 (0.03)	3.03 (0.04)	3.16 (0.01)	3.39 (0.01)	3.58 (0.07)	-
<b>E (3.85)</b>	2.77 (0.01)	2.89 (0.04)	-	3.65 (0.05)		-
<b>E (3.69)</b>	2.78 (0.02)	2.91 (0.05)	-	3.65 (0.06)	3.84 (0.01)	-
<b>E (3.54)</b>	2.79 (0.01)	2.93 (0.06)	-	3.60 (0.03)	3.72 (0.02)	-
	<i>Refined XAS Data</i>					
<b>Inactive</b>	2.84 [3.3]	2.95 [2.3]	3.14 [1.2]	3.53 [1.6]	3.71 [0.4]	4.24 [0.8]
<b>Active</b>	2.83 [1.8]	2.95 [2.0]	3.12 [1.2]	3.49 [0.4]	3.79 [0.3]	4.27 [0.2]

<sup>a</sup>Refined analysis of calculated and measured Mn–Mn distances. As detailed in the text, the Mn–Mn 1 and Mn–Mn 2 shells are both partitioned in three subshells, approximately corresponding to (Mn–Mn 1a) Mn–Mn pairs linked through non-protonated  $\mu_2$ -O and  $\mu_3$ -O bridges; (Mn–Mn 1b) Mn–Mn pairs linked through protonated  $\mu_2$ -OH bridges; (Mn–Mn 1c) Mn(III)–Mn(IV) pairs belonging to complete cubane-like units; (Mn–Mn 2a) out-of-plane Mn atom linked to in plane Mn atom through oxo bridge non-involved in JT distortion; (Mn–Mn 2b) out-of-plane Mn atom linked to in plane Mn atom through oxo bridge involved in JT distortion; (Mn–Mn 2c) linear “rocksalt-like” Mn–O–Mn motif involving complete cubane-like units. Theoretical values are related to the A–E clusters discussed in the text, having different average oxidation states of the Mn atoms. Data have been averaged on different distances of the same type, and standard deviations ( $\sigma$ ) are reported in round brackets. XAS results shown in Figure 7 have been also summarized at the end of the table. Square brackets contain coordination numbers obtained by EXAFS simulations in the case of XAS data; further details can be found in the Supporting Information.



**Figure 7.** Refined Fourier transformed EXAFS spectra for the active (AF) and inactive (IF) MnCat films. Experimental and simulated EXAFS spectra are shown as inset. The experimental data are shown in black and the simulated spectra in color. Simulation parameters are given in Table S2 (refined simulation approach).

distances in both the active and inactive films. An overall greater abundance of Mn–Mn nearest neighbors in the inactive film is striking in the case of the subshell 1a (2.83–2.84 Å), indicating the presence of a thick network of nonprotonated  $\mu_2$ -O and  $\mu_3$ -O bridges in line with the formation of larger Mn-oxo sheets in the inactive film than in the active film. This indication is also compatible with a similarly higher number of coordination found in the case of Mn–Mn 3 and Mn–Mn 4 distances (see Table 1). On the contrary, the almost perfect equivalence of the subshells 1b (2.95 Å) and 1c (3.12–3.14 Å) indicates that protonated  $\mu_2$ -OH sites and complete cubane units can be equally found in both the films. The Mn–Mn 2 shell (3.5–3.8 Å) contains the fingerprints of all the atomistic motifs which involves Mn atoms not belonging to the Mn-oxo sheets. However, it does not offer special information on the structural differences between active and inactive films: complete cubane units which form near the boundaries of the Mn-oxo sheets, as in the case of cluster C (see 2c in Table 3), as well as Mn adatoms found in the case of the B, D and E

clusters, are present in both films but they are more abundant in the inactive film and should be therefore hardly considered as key active sites for oxygen evolution. The Mn–O shell provides instead valuable information on the distribution and properties of Mn(III) atoms, which are preferred sites for the subtraction of electrons during the oxygen evolution reaction, when the catalyst film is exposed to an external positive potential. Our calculations reveal that the strong JT distortion of the Mn(III)O<sub>6</sub> octahedra is favored in the case of Mn atoms placed at the catalyst/water interface, because of the easier relaxation of the Mn–OH<sub>2</sub> terminations. A greater amount of Mn(III) sites is found in the active catalyst, and the longer Mn–O c distance found in the case of the inactive film should not mislead the interpretation of the results: a smaller amount of Mn(III) in the inactive film, accompanied by an involvement of  $\mu_2$ -O and  $\mu_3$ -O bridges in the JT distortion, preserves the full 6-fold-coordination of Mn atoms even in a distorted geometry. The active catalyst is likely composed by smaller units, and it is therefore characterized by a greater amount of terminal Mn–OH<sub>2</sub> species. Water molecules are basically not anymore bonded to interfacial Mn(III) sites and cannot be detected by XAS measurements, resulting in a lower overall coordination of the Mn–O network. All of these findings suggest that more active films are quantitatively rather than qualitatively different from less active oxides and that there are no clearly eligible sites for oxygen evolution in MnCat, similar to what has been already discussed in the case of the CoCat.<sup>41</sup> The amorphous Mn-oxo network is likely characterized by a diffuse capability of localizing oxidizing holes at Mn(III) sites, either placed at the boundary of planar sheets or belonging to cubane units. The reshuffling of protons through low-barrier H bonds, which is an inherent property of the H–O–H...O–H structures present in all the proposed MnCat models, can offer then an easy route to the formation of primary intermediates (e.g., Mn(IV)=O<sup>•</sup> species) of oxygen evolution.

#### 4. CONCLUSIONS

We obtained major progress toward detailed insight into the atomic structure and electronic properties of a Mn-based amorphous oxide catalyst for water oxidation (MnCat) by combining the information content of XAFS data with the predictive power of ab initio calculations. This combination became possible only by development of an accurate DFT approach that solves a long-standing methodological problem, namely the quantitative determination of Mn–O and Mn–Mn fingerprint distances at an accuracy that matches the precision of the XAFS experiment. Our DFT/XAFS fingerprint approach for structure elucidation immediately facilitated identification of several structural motifs present in several families of water-oxidizing manganese oxides as well as insight in the distribution of protons at the MnCat/water interface and in the localization of Mn(II), Mn(III), and Mn(IV) ions in the amorphous oxides. Our results indicate, in particular, that more active catalyst films are formed by the interconnection of small planar Mn-oxo sheets cross-linked through different kinds of out-of-plane Mn atoms, isolated, or arranged in closed cubane-like units. As opposed to the relatively inactive Mn oxides investigated here, containing larger sheets and more organized units mostly formed by Mn(IV)O<sub>6</sub> blocks, active films contain a relevant amount of defective Mn(III)O<sub>5</sub> units placed at the boundary of the amorphous network, where they are ready to act as hole traps that trigger the oxidation of neighboring water molecules and the subsequent oxygen evolution reaction when the catalyst

is exposed to an external positive potential. Finally, the validation of sound 3D models of the atomic structure, protonation, and oxidation-state localization of MnCat opens the way to the development of mechanistic models of its functioning which go beyond a speculative level.

#### ■ ASSOCIATED CONTENT

##### Supporting Information

The Supporting Information is available free of charge on the ACS Publications website at DOI: 10.1021/jacs.5b05174.

Additional details of XAS measurements and analyses; pyrolusite MnO<sub>2</sub> and monoclinic Ca<sub>2</sub>Mn<sub>3</sub>O<sub>8</sub> periodic crystals; complete summary of the structural properties of the investigated Mn<sub>6</sub>–Mn<sub>20</sub> clusters; periodic Mn-oxo Sheets; magnetic coupling of Mn centers; Bader and Lowdin charge analysis of the E1 (3.69) cluster (PDF)

#### ■ AUTHOR INFORMATION

##### Corresponding Author

\*giuseppe.mattioli@ism.cnr.it

##### Notes

The authors declare no competing financial interest.

#### ■ ACKNOWLEDGMENTS

We acknowledge computational resources provided by the Caliban-HPC computer center of the University of L'Aquila. Furthermore, L.G. acknowledges funding provided by the European Research Council project no. 240624 within the VII Framework Program of the European Union. Support by the Deutsche Forschungsgemeinschaft (DFG) to the Berlin Cluster of Excellence on Unifying Concepts in Catalysis (EXL 31411) and to the Collaborative Research Center 1078 (project A4) is gratefully acknowledged. We also thank the Bundesministerium für Bildung und Forschung (MEOKAT project, 03SF0433B) for financial support. We thank Dr. F. Schäfers, M. Mertin, and M. Gorgoi for technical support at the beamline KMC-1 of the BESSY synchrotron operated by the Helmholtz-Zentrum Berlin (HZB).

#### ■ REFERENCES

- (1) Barber, J. *Chem. Soc. Rev.* **2009**, 38, 185.
- (2) Dau, H.; Zaharieva, I.; Haumann, M. *Curr. Opin. Chem. Biol.* **2012**, 16, 3.
- (3) Najafpour, M. M.; Moghaddam, A. N.; Shen, J.-R.; Govindjee. In *Stress Biology of Cyanobacteria*; Srivastava, A. et al., Eds.; CRC Press, Taylor & Francis Group: Boca Raton, FL, 2013, 41–60.
- (4) Najafpour, M. M.; Moghaddam, A. N.; Allakhverdiev, S. I.; Govindjee. *Biochim. Biophys. Acta, Bioenerg.* **2012**, 1817, 1110–1121.
- (5) *Natural and Artificial Photosynthesis: Solar Power as an Energy Source*; Razeghifard, R., Ed.; John Wiley & Sons: Hoboken, NJ, 2013.
- (6) *Current challenges in photosynthesis: From natural to artificial*. Hou, H. J. M., Allakhverdiev, S. I., Najafpour, M. M., Govindjee, Eds.; Frontiers Research Topic; Ebook, Frontiers Media, Lausanne, Switzerland, 2014.
- (7) Microbial BioEnergy: Hydrogen Production. In *Advances in Photosynthesis and Respiration Series*; Zannoni, D., De Philippis, R., Eds.; Springer, Dordrecht, 2014; Vol. 38.
- (8) Reece, S. Y.; Hamel, J. A.; Sung, K.; Jarvi, T. D.; Esswein, A. J.; Pijpers, J. J. H.; Nocera, D. G. *Science* **2011**, 334, 645–648.
- (9) Nocera, D. G. *Acc. Chem. Res.* **2012**, 45, 767.
- (10) Tachibana, Y.; Vayssieres, L.; Durrant, J. R. *Nat. Photonics* **2012**, 6, 511.
- (11) Kanan, M. W.; Nocera, D. G. *Science* **2008**, 321, 1072.

- (12) Dau, H.; Limberg, C.; Reier, T.; Risch, M.; Roggan, S.; Strasser, P. *ChemCatChem* **2010**, *2*, 724.
- (13) Kwabena Bediako, D.; Lassalle-Kaiser, B.; Surendranath, Y.; Yano, J.; Yachandra, V. K.; Nocera, D. G. *J. Am. Chem. Soc.* **2012**, *134*, 6801.
- (14) Zaharieva, I.; Chernev, P.; Risch, M.; Klingan, K.; Kohlhoff, M.; Fischer, A.; Dau, H. *Energy Environ. Sci.* **2012**, *5*, 7081.
- (15) Liu, X.; Wang, F. *Coord. Chem. Rev.* **2012**, *256*, 1115.
- (16) Smith, R. D. L.; Prévot, M. S.; Fagan, R. D.; Zhang, Z.; Sedach, P. A.; Siu, M. K. J.; Trudel, S.; Berlinguette, C. P. *Science* **2013**, *340*, 60–63.
- (17) Hambourger, M.; Moore, G. F.; Kramer, D. M.; Gust, D.; Moore, A. L.; Moore, T. A. *Chem. Soc. Rev.* **2009**, *38*, 25.
- (18) Umena, Y.; Kawakami, K.; Shen, J.-R.; Kamiya, N. *Nature* **2011**, *473*, 55–60.
- (19) Suga, M.; Akita, F.; Hirata, K.; Ueno, G.; Murakami, H.; Nakajima, Y.; Shimizu, T.; Yamashita, K.; Yamamoto, M.; Ago, H.; Shen, J.-R. *Nature* **2014**, *517*, 99–103.
- (20) Wiechen, M.; Najafpour, M. M.; Allakhverdiev, S. I.; Spiccia, L. *Energy Environ. Sci.* **2014**, *7*, 2203–2212.
- (21) Ramirez, A.; Bogdanoff, P.; Friedrich, D.; Fiechter, S. *Nano Energy* **2012**, *1*, 282–289.
- (22) Wiechen, M.; Zaharieva, I.; Dau, H.; Kurz, P. *Chem. Sci.* **2012**, *3*, 2330–2339.
- (23) Bergmann, A.; Zaharieva, I.; Dau, H.; Strasser, P. *Energy Environ. Sci.* **2013**, *6*, 2745–2755.
- (24) Gorlin, Y.; Lassalle-Kaiser, B.; Benck, J. D.; Gul, S.; Webb, S. M.; Yachandra, V. K.; Yano, J.; Jaramillo, T. F. *J. Am. Chem. Soc.* **2013**, *135*, 8525–8534.
- (25) Park, J.; Kim, H.; Jin, K.; Lee, B. J.; Park, Y.-S.; Kim, H.; Park, I.; Yang, K. D.; Jeong, H.-Y.; Kim, J.; Hong, K. T.; Jang, H. W.; Kang, K.; Nam, K. T. *J. Am. Chem. Soc.* **2014**, *136*, 4201–4211.
- (26) Meng, Y.; Song, W.; Huang, H.; Ren, Z.; Chen, S.-Y.; Suib, S. L. *J. Am. Chem. Soc.* **2014**, *136*, 11452–11464.
- (27) Bloor, L. G.; Molina, P. I.; Symes, M. D.; Cronin, L. *J. Am. Chem. Soc.* **2014**, *136*, 3304–3311.
- (28) Najafpour, M.; Moghaddam, A.; Dau, H.; Zaharieva, I. *J. Am. Chem. Soc.* **2014**, *136*, 7245–7248.
- (29) Hocking, R. K.; Malaeb, R.; Gates, W. P.; Patti, A. F.; Chang, S. L. Y.; Devlin, G.; MacFarlane, D. R.; Spiccia, L. *ChemCatChem* **2014**, *6*, 2028–2038.
- (30) Ansell, G. B.; Modrick, M. A.; Longo, J. M.; Poeppelmeier, K. R.; Horovitz, H. S. *Acta Crystallogr., Sect. B: Struct. Crystallogr. Cryst. Chem.* **1982**, *38*, 1795–1797.
- (31) Post, J. E. *Proc. Natl. Acad. Sci. U. S. A.* **1999**, *96*, 3447–3454.
- (32) Webb, S. M.; Tebo, B. M.; Bargar, J. R. *Am. Mineral.* **2005**, *90*, 1342–1357.
- (33) Manceau, A.; Marcus, M. A.; Grangeon, S.; Lanson, M.; Lanson, B.; Gaillot, A.-C.; Skanthakumar, S.; Soderholm, L. *J. Appl. Crystallogr.* **2013**, *46*, 193–209.
- (34) Zaharieva, I.; Najafpour, M. M.; Wiechen, M.; Haumann, M.; Kurz, P.; Dau, H. *Energy Environ. Sci.* **2011**, *4*, 2400–2408.
- (35) Risch, M.; Khare, V.; Zaharieva, I.; Gerencser, L.; Chernev, P.; Dau, H. *J. Am. Chem. Soc.* **2009**, *131*, 6936.
- (36) Kanan, M. W.; Yano, J.; Surendranath, Y.; Dinca, M.; Yachandra, V. K.; Nocera, D. G. *J. Am. Chem. Soc.* **2010**, *132*, 13692.
- (37) Du, P.; Kokhan, O.; Chapman, K. W.; Chupas, P. J.; Tiede, D. M. *J. Am. Chem. Soc.* **2012**, *134*, 11096.
- (38) Mattioli, G.; Risch, M.; Amore Bonapasta, A.; Dau, H.; Guidoni, L. *Phys. Chem. Chem. Phys.* **2011**, *13*, 15437.
- (39) Hu, X. L.; Piccinin, S.; Laio, A.; Fabris, S. *ACS Nano* **2012**, *6*, 10497–10504.
- (40) Wang, L.-P.; Van Voorhis, T. *J. Phys. Chem. Lett.* **2011**, *2*, 2200.
- (41) Mattioli, G.; Giannozzi, P.; Amore Bonapasta, A.; Guidoni, L. *J. Am. Chem. Soc.* **2013**, *135*, 15353–15363.
- (42) Li, X.; Siegbahn, P. E. M. *J. Am. Chem. Soc.* **2013**, *135*, 13804–13813.
- (43) Risch, M.; Klingan, K.; Ringleb, F.; Chernev, P.; Zaharieva, I.; Fischer, A.; Dau, H. *ChemSusChem* **2012**, *5*, 542.
- (44) Giannozzi, P.; Baroni, S.; Bonini, N.; Calandra, M.; Car, R.; Cavazzoni, C.; Ceresoli, D.; Chiarotti, G. L.; Cococcioni, M.; Dabo, I.; de Gironcoli, S.; Fabris, S.; Fratesi, G.; Gebauer, R.; Gerstmann, U.; Gougoussis, C.; Kokalj, A.; Lazzeri, M.; Martin-Samos, L.; Marzari, N.; Mauri, F.; Mazzarello, R.; Paolini, S.; Pasquarello, A.; Paulatto, L.; Sbraccia, C.; Scandolo, S.; Sclauzero, G.; Seitsonen, A. P.; Smogunov, A.; Umari, P.; Wentzcovitch, R. *J. Phys.: Condens. Matter* **2009**, *21*, 3865–3868.
- (45) Kresse, G.; Joubert, D. *Phys. Rev. B: Condens. Matter Mater. Phys.* **1999**, *59*, 1758–1775.
- (46) Louie, S. G.; Froyen, S.; Cohen, M. L. *Phys. Rev. B: Condens. Matter Mater. Phys.* **1982**, *26*, 1738–1742.
- (47) Dal Corso, A. *Comput. Mater. Sci.* **2014**, *95*, 337–350.
- (48) Perdew, J. P.; Burke, K.; Ernzerhof, M. *Phys. Rev. Lett.* **1996**, *77*, 3865–3868.
- (49) Kulik, H. J.; Cococcioni, M.; Scherlis, D. A.; Marzari, N. *Phys. Rev. Lett.* **2006**, *97*, 103001.
- (50) Cao, C.; Hill, S.; Cheng, H.-P. *Phys. Rev. Lett.* **2008**, *100*, 167206.
- (51) Hsu, H.; Umemoto, K.; Cococcioni, M.; Wentzcovitch, R. *Phys. Rev. B: Condens. Matter Mater. Phys.* **2009**, *79*, 125124.
- (52) Mattioli, G.; Alippi, P.; Filippone, F.; Caminiti, R.; Amore Bonapasta, A. *J. Phys. Chem. C* **2010**, *114*, 21694.
- (53) Himmetoglu, B.; Floris, A.; de Gironcoli, S.; Cococcioni, M. *Int. J. Quantum Chem.* **2014**, *114*, 14–49.
- (54) Cohen, A. J.; Mori-Sánchez, P.; Yang, W. *Science* **2008**, *321*, 792–794.
- (55) Cococcioni, M.; de Gironcoli, S. *Phys. Rev. B: Condens. Matter Mater. Phys.* **2005**, *71*, 035105.
- (56) Norman, M. R.; Freeman, A. J. *Phys. Rev. B: Condens. Matter Mater. Phys.* **1986**, *33*, 8896.
- (57) McMahan, A. K.; Martin, R. M.; Satpathy, S. *Phys. Rev. B: Condens. Matter Mater. Phys.* **1988**, *38*, 6650.
- (58) Becke, A. D. *J. Chem. Phys.* **1993**, *98*, 5648–5652.
- (59) Lee, C.; Yang, W.; Parr, R. G. *Phys. Rev. B: Condens. Matter Mater. Phys.* **1988**, *37*, 785–789.
- (60) Scherlis, D. A.; Cococcioni, M.; Sit, P.; Marzari, N. *J. Phys. Chem. B* **2007**, *111*, 7384–7391.
- (61) Mori-Sánchez, P.; Cohen, A. J.; Yang, W. *Phys. Rev. Lett.* **2009**, *102*, 066403.
- (62) Neese, F. *WIREs Comput. Mol. Sci.* **2012**, *2*, 73–78.
- (63) Schäfer, A.; Horn, H.; Ahlrichs, R. *J. Chem. Phys.* **1992**, *97*, 2571–2577.
- (64) Weigend, F.; Ahlrichs, R. *Phys. Chem. Chem. Phys.* **2005**, *7*, 3297–3305.
- (65) ECP parameters and basis sets for Mn[SD(10,MDF)] and O[SD(2,MWB)] pseudopotentials have been obtained from the pseudopotential library of the Stuttgart/Cologne group: <http://www.tc.uni-koeln.de/PP/clickpse.en.html>.
- (66) Penner-Hahn, J. E. *Coord. Chem. Rev.* **1999**, *190-192*, 1101–1123.
- (67) Rehr, J. J.; Albers, R. C. *Rev. Mod. Phys.* **2000**, *72*, 621.
- (68) Ankudinov, A. L.; Ravel, B.; Rehr, J. J.; Conradson, S. D. *Phys. Rev. B: Condens. Matter Mater. Phys.* **1998**, *58*, 7565.
- (69) Ramesh, T. N.; Kamath, P. V.; Shivakumara, C. *Acta Crystallogr., Sect. B: Struct. Sci.* **2006**, *62*, 530–536.
- (70) Capehart, T. W.; Corrigan, D. A.; Conell, R. S.; Pandya, K. I.; Hoffman, R. W. *Appl. Phys. Lett.* **1991**, *58*, 865–867.
- (71) Glemser, O.; Einerhand, J. Z. *Anorg. Chem.* **1950**, *261*, 43–51.
- (72) Johnston, W. D.; Heikes, R. R.; Sestrich, D. *J. Phys. Chem. Solids* **1958**, *7*, 1.
- (73) Shao-Horn, Y.; Hackney, S. A.; Kahaian, A. J.; Thackeray, M. M. *J. Solid State Chem.* **2002**, *168*, 60.
- (74) Delaplane, R. G.; Ibers, J. A.; Ferraro, J. R.; Rush, J. J. *J. Chem. Phys.* **1969**, *50*, 1920–1927.
- (75) Jahn, H. A.; Teller, E. *Proc. R. Soc. London, Ser. A* **1937**, *161*, 220–235.
- (76) Shriver, D. F.; Atkins, P. W. *Inorganic Chemistry*, 3rd ed.; Oxford University Press: London, 1999.

(77) Afrati, T.; Dendrinou-Samara, C.; Raptopoulou, C. P.; Terzis, A.; Tangoulis, V.; Kessissoglou, D. P. *Angew. Chem., Int. Ed.* **2002**, *41*, 2148–2150.

(78) Alexiou, M.; Dendrinou-Samara, C.; Karagianni, A.; Biswas, S.; Zaleski, C. M.; Kampf, J.; Yoder, D.; Penner-Hahn, J. E.; Pecoraro, V. L.; Kessissoglou, D. P. *Inorg. Chem.* **2003**, *42*, 2185–2187.

(79) A complete survey of Mn–O and Mn–Mn distances of all the investigated systems is reported in the [Supporting Information](#).

(80) The same analysis performed on the B3LYP structures of the A–C clusters provides results in close agreement with DFT+U.

(81) Surendranath, Y.; Kanan, M. W.; Nocera, D. G. *J. Am. Chem. Soc.* **2010**, *132*, 16501.